# Experimental and Theoretical Studies on the Controlled Synthesis of Alkali-Metal-Doped Rare-Earth Oxysulfide Nanocrystals

Tao Zhang, Jun Gu, Yi Ding, Ya-Wen Zhang,* and Chun-Hua Yan*[a]

Alkali-metal (Li, Na, K)-doped lanthanum oxysulfide nanoplates were obtained in the hexagonal phase by thermolysis of metal acetylacetonates in organic solvents with high boiling points and sulfurization using sulfur powders. The characterization results showed that the size, shape, crystallinity, composition, and phase stability of the $La_2O_2S$ nanocrystals were affected by the doped alkali metals. Combined with first-principles calculations of the formation energy of anionic defects in the lattices, the ternary phase diagrams for the formation of rare-earth oxysulfides ($RE_2O_2S$) were calculated. Both the experimental results and the phase diagrams have demonstrated that the doped alkali metals are capable of promoting the formation of $RE_2O_2S$ nanocrystals in the order of K≈Na>Li. With K acting as the doping alkali metal, the phase-formation capability for different $RE_2O_2S$ (e.g., Eu, Gd, Yb, Lu) along the lanthanide series was also explored under the guidance of the hard and soft acid and base (HSAB) theory. Moreover, the as-developed synthetic route could be applied also to the production of K/Eu- and K/Tb-codoped $La_2O_2S$ nanoplates, which displayed intense red and green emissions, respectively, under ultraviolet-light excitations.

## Introduction

Rare-earth (RE) compounds with versatile material properties originating from the unique 4f electron configuration of lanthanide elements have been used widely in many important fields such as optics, magnetics, electronics, and catalysis.[1] With the rapidly expanding development of nanoscience and nanotechnology over the last two decades, rare-earth-based functional nanocrystals (NCs) have become an important field of research among nanomaterials with multidisciplinary applications.

Over the past few years, the synthesis of monodispersed rare-earth compound NCs such as oxides ($RE_2O_3$),[2a,b,c] fluorides ($REF_3$),[2d,e] oxyfluorides (REOF),[2e,f,g] oxychlorides (REOCl),[2h] alkali- and alkaline-earth-metal complex salts ($NaREF_4$, $BaREF_5$),[3a,b,c] divalent sulfides (EuS),[3d,e] oxysulfides ($RE_2O_2S$),[3f,g,h,j] and alkali-metal sulfide complex salts ($NaRES_2$)[3i] have been realized by various organic-phase-based thermolysis methods in surfactant solutions. Our previous study indicated that the hard and soft acid and base (HSAB) theory[4] seems to give good predictions in the formation trend of various kinds of rare-earth NCs:[3h,i,j] as typical hard acids, $RE^{3+}$ ions have a strong affinity to typical hard bases such as fluoride ions ($F^-$)

or oxygen ions ($O^{2-}$), which facilitate the formation of oxide and fluoride NCs; whereas for softer bases such as chloride ions ($Cl^-$) or sulfur ions ($S^{2-}$), the affinity becomes weaker, which leads to the demanding synthetic conditions required to form sulfide or chloride NCs.

Rare-earth oxysulfide ($RE_2O_2S$) is well known as a kind of high-performance luminescence material of significant applications.[5] A typical synthetic method for bulk oxysulfide concerns reacting a rare-earth oxide ($RE_2O_3$) with vulcanization reagents (such as $Na_2S_2O_3$, thiourea, etc.).[6] Previously, Gao's group synthesized $RE_2O_2S$ (RE = Eu, Gd, Tb) nanoplates by using a thermal decomposition method with single-source precursor in the organic phase.[3f,g] More recently, our group demonstrated that highly monodispersed $RE_2O_2S$ NCs could be obtained by means of a thermolytic approach in organic solvents with high boiling points, with sodium as the doping element.[3h]

Herein, we report the controlled synthesis of $RE_2O_2S$ NCs doped by different alkali metals (Li, Na, and K) through the combination of well-designed experiments and density functional theory (DFT) simulations. Our results show that the doping of alkali metals into $RE_2O_2S$ not only affects the size, shape, composition, and crystallinity of the NCs, but also plays an important role in stabilizing the structure of the $RE_2O_2S$ host, thereby showing a sequence of K≈Na>Li in stabilizing capability. By following the developed method, highly luminescent Eu/K- and Tb/K-codoped $RE_2O_2S$ NCs could be also prepared.

[a] T. Zhang, J. Gu, Y. Ding, Prof. Dr. Y.-W. Zhang, Prof. Dr. C.-H. Yan
Beijing National Laboratory for Molecular Sciences
State Key Laboratory of Rare Earth Materials Chemistry and
Applications, College of Chemistry and Molecular Engineering
Peking University, Beijing 100871 (P.R. China)
Fax: (+86) 10-6275-6787
E-mail: ywzhang@pku.edu.cn
yan@pku.edu.cn

Supporting information for this article is available on the WWW under
http://dx.doi.org/10.1002/cplu.201300092.

## Results and Discussion

In this study, alkali-metal-doped $La_2O_2S$ NCs were prepared by using rare-earth acetylacetonate and alkali-metal acetylacetonate as metal precursors, a mix of oleic acid (OA), oleylamine (OM), and 1-octadecene (ODE) as the solvent, and sublimed sulfur as the sulfur source. By using this method, lithium-doped $La_2O_2S$ NCs were firstly synthesized (Figure 1). The trans-
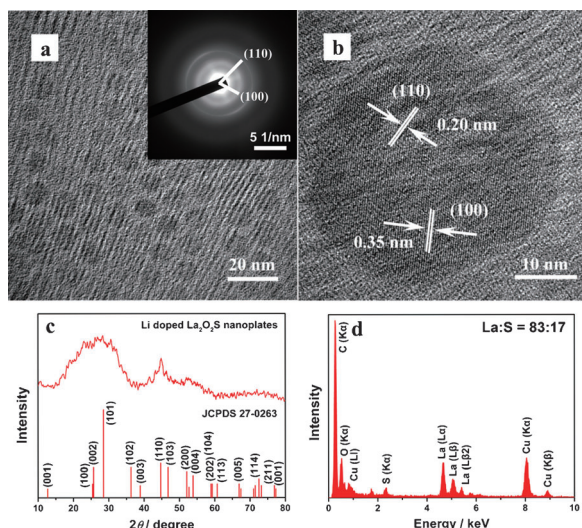


**Figure 1.** a) TEM image and SAED pattern (inset) of Li-doped $La_2O_2S$ NCs and b) HRTEM image of a single $La_2O_2S$ nanocrystal. c) XRD pattern and d) EDS spectrum of Li-doped $La_2O_2S$ NCs. The standard XRD pattern of hexagonal $La_2O_2S$ (JCPDS 27-0263) is also shown in panel (c) for reference.

mission electron microscopy (TEM) measurements showed that the Li-doped NCs had a hexagonal-plate structure with the size of $(8.9\pm0.8)\times(1.7\pm0.2)$ nm (Figure 1a and Table 1). As observed by high-resolution transmission electron microscopy (HRTEM), the lattice fringes on a single Li–$La_2O_2S$ nanoplate are blurring, suggestive of the low crystallinity of the NCs. However, lattice fringe spacings of 0.35 and 0.20 nm corresponding to the (100) and (111) crystal planes of $La_2O_2S$, respectively, could still be distinguished for this sample (Figure 1b). X-ray diffraction (XRD) and energy-dispersive X-ray analysis spectroscopy (EDS) were further used to determine the crystal structure and chemical composition of this sample, respectively (Fig-

ure 1c,d). In comparison with the standard pattern (JCPDS 27-0263) of hexagonal $La_2O_2S$, the rather weak intensity and considerably broadened contours of the XRD peaks indicated that the Li-doped $La_2O_2S$ NCs were crystallized poorly and had an ultra-small size along the (002) facet (c axis; Figure 1c), which is in accordance with the results of TEM and selected-area electron diffraction (SAED) analysis. The EDS analysis indicated that the La/S ratio for Li-doped NCs was 4.9:1 (Figure 1d, Table 1), higher than that (2.6:1) for Na-doped NCs,[3h] which demonstrates that the lower content of S atoms could be introduced into the lattice in the presence of Li dopant. These results strongly suggest that Li might not be as effective as Na in promoting the formation of lanthanide oxysulfide NCs.

Potassium-doped $La_2O_2S$ NCs were synthesized by the same method by using potassium acetylacetonate as the doping reagent (Figure 2). K-doped $La_2O_2S$ NCs also showed the hexago-
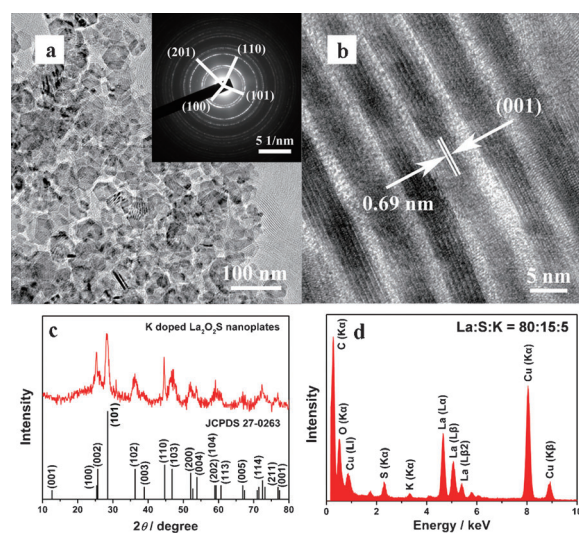


**Figure 2.** a) TEM image and SAED pattern (inset) of K-doped $La_2O_2S$ NCs. b) HRTEM image of K-doped $La_2O_2S$ NCs standing on the side plane. c) XRD pattern and (d) EDS spectrum of K-doped $La_2O_2S$ NCs. The standard XRD pattern of $La_2O_2S$ (JCPDS no. 27-0263) is also shown in panel (c) for reference.

nal-plate morphology, although the average size $((46.2\pm7.6)\times(4.5\pm0.4)$ nm)) of the nanoplates was much larger than that of Li-doped $La_2O_2S$ NCs (Figure 2a and Table 1). The observation of intense diffraction rings from the SAED pattern (corresponding to the crystal planes of (100), (101), (110), and (201) of hexagonal $La_2O_2S$) demonstrated a higher crystallinity of the K-doped NCs than the Li-doped ones (see insets in Figures 1a and 2a). When the concentration of the NCs in the cyclohexane dispersant was higher, the solvent-induced self-assembly structure with the face-to-face formation was observed for the nanoplates on the TEM grid. This allows the nanoplates to orient perpendicularly to the carbon film of the grid and facilitates the HRTEM observation from the side plane of the nanoplates. Figure 2b indicates that the interplanar spacing is 0.69 nm, which corresponds to the (001) direction of the K-doped $La_2O_2S$ NCs. XRD characterization further confirmed that

**Table 1.** Size, composition, and morphology of alkali-metal-doped $RE_2O_2S$ NCs.

| M-$RE_2O_2S$ | Dimensions [nm] | Atomic ratio | | Morphology |
| --- | --- | --- | --- | --- |
| | | La/M | La/S | |
| Li-$La_2O_2S$ | $(8.9\pm0.8)\times(1.7\pm0.2)$ | – | 4.9:1 | hexagonal plates |
| Na-$La_2O_2S$[a] | $(22.3\pm2.0)\times(2.1\pm0.2)$ | 3.8:1 | 2.6:1 | hexagonal plates |
| K-$La_2O_2S$ | $(46.2\pm7.6)\times(4.5\pm0.4)$ | 16:1 | 5.2:1 | hexagonal plates |
| K-$Eu_2O_2S$ | $(13.5\pm1.8)$ | 15:1 | 4.0:1 | irregular plates |
| K-$Gd_2O_2S$ | $(10.9\pm1.7)$ | 15:1 | 3.5:1 | irregular plates |
| K-$Yb_2O_2S$ | $(1.0\pm0.1)$ | 11:1 | 4.2:1 | small particles |
| [a] The relevant data of Na-doped $La_2O_2S$ is from Ref. [3h]. | | | | |

the K-doped $La_2O_2S$ NCs were highly crystallized and showed a hexagonal crystal structure. The unit-cell parameters ($a = 4.074$ Å, $c/a = 1.727$, $V = 101.1$ Å$^3$) were obtained by least-squares methods, and were larger than those of standard $La_2O_2S$ (JCPDS 27-0263, $a = 4.050$ Å, $c/a = 1.714$, $V = 98.61$ Å$^3$). As determined by EDS analysis (Figure 2d), the La/S ratio is 5.2:1 for the K-doped $La_2O_2S$ NCs, rather greater than that (La/S 2:1) for bulk $La_2O_2S$, which indicates that insufficient S atoms were included in the nanoplate structure during the doping process with potassium. Both SAED and XRD observations suggested that K might act as a more effective stabilizing agent in the formation of highly crystallized $La_2O_2S$ NCs (Figure 1a,c and 2a,c).

The sizes, compositions, and shapes of alkali-metal-doped $La_2O_2S$ NCs are listed in Table 1. From Li to Na and to K, the hexagonal nanoplates tended to grow bigger along with enhanced crystallinity. This directly proves that K or Na has a more powerful capability in stabilizing $La_2O_2S$ NCs than Li.[3h] It is also seen that the alkali-metal doping amount decreases when the doping element turns from Na to K. It is worth mentioning that there is no monotonous trend of the composition ratio between La and S. Both Li- and K-doped NCs show a decrease in the sulfur content. We speculate that there are different reasons for the decreases. For Li-doped $La_2O_2S$, the elemental ratio is affected by the thickness of the hexagonal nanoplates. Our previous study proved that $La^{3+}$ acts as the end ion on both sides of the nanoplates.[3h] The thinner the nanoplates become, the higher the proportion of surface La atoms. This allows the ratio between La and S to increase. For K-doped $La_2O_2S$, the elemental ratio is related to two factors: nanoplate thickness and sulfur vacancy. The existence of sulfur vacancies plays a key role in the reduction of the sulfur content. The relationship between the defect-formation energies of different anion vacancies was confirmed to be influenced by the proportion of sulfur present, as calculated by DFT as discussed below.

As is known, $La_2O_2S$ belongs to the hexagonal system and $P\bar{3}m1$ space group. There is one $La_2O_2S$ in the unit cell with the following coordinates of the respective atoms: La (0.667, 0.333, 0.279) and (0.333, 0.667, 0.721), O (0.667, 0.333, 0.629) and (0.333, 0.667, 0.371), and S (0, 0, 0). The Vienna ab initio simulation package (VASP) was chosen to perform the DFT simulations. The generalized gradient approximation (GGA) Perdew–Burke–Ernzerhof (PBE) exchange-correlation functional was utilized to calculate the defect-formation energy, and the projector augmented-wave (PAW) pseudopotential was used to describe the interaction between the ion core and valence electrons. The K-space cut-off energy was set to 450 eV. By using the Brillouin zone integral with a $5 \times 5 \times 3$ Monkhorst-Pack grid point in $k$ space, the original unit cell was relaxed to obtain the most stable structure. To better calculate the defect-formation energy, we adopted the supercell model[7] in which a $2 \times 2 \times 1$ supercell was established (left part of Figure 3). The same method was also used for $La_2O_3$ (JCPDS 40-1279, $a = 4.039$ Å, $c/a = 1.585$; right part of Figure 3).

A preliminary study[3h] has shown that there is a quantitative relationship between the phase formation of different NCs (i.e.,
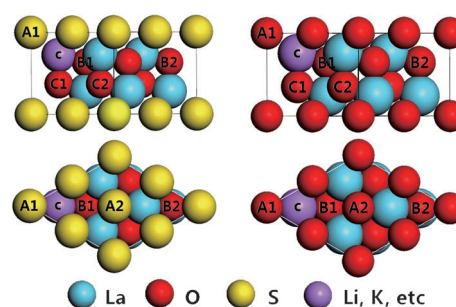


**Figure 3.** Lateral and top view of the $La_2O_2S$ (left) and $La_2O_3$ (right) $2 \times 2 \times 1$ supercell structures. The sky blue positions represent doping atoms. The atoms with black tags represent the possible positions of anion defects.

$La_2O_2S$ and $La_2O_3$) and the chemical potential of monomers (i.e., O and S). The reaction system should meet the following conditions to guarantee the phase of $La_2O_2S$: firstly, the chemical potential of the monomers in the solution should not be higher than that of the most stable simple substance. Here we define the chemical potential of the most stable simple substance as zero, therefore the chemical potential of the monomers must be less than zero, or otherwise simple substances will precipitate from the system; secondly, in the system of the three elements—La, O, and S—there are three possible compounds, which may generate $La_2O_3$, $La_2O_2S$, and $La_2S_3$. To obtain stable $La_2O_2S$ NCs, the chemical potential of each substance should satisfy the following relationship [Eq. (1)].

$$2\mu_{La} + 2\mu_O + \mu_S = \mu_{La_2O_2S} \tag{1a}$$

$$2\mu_{La} + 3\mu_O < \mu_{La_2O_3} \tag{1b}$$

$$2\mu_{La} + 3\mu_S < \mu_{La_2S_3} \tag{1c}$$

According to the single-point energy of each substance, the phase diagram of the ternary system was determined by regarding the chemical potential of O and S as the vertical and horizontal coordinates, respectively. The phase boundary was defined by the chemical-conversion relationship between $La_2O_3$ and $La_2O_2S$ [Eq. (2)].

$$La_2O_2S + O \rightarrow La_2O_3 + S \tag{2}$$

Equation (2) could be expressed by the single-point energy of the compounds as well as the chemical potential of the simple substance [Eq. (3)]:

$$\mu_O = \mu_S + E_{tot}(La_2O_2S) - E_{tot}(La_2O_3) \tag{3}$$

According to Equation (3), the phase boundary is a straight line with a slope equal to 1. A preliminary study[3h] had shown the stable conditions for $La_2O_2S$ NCs to be as follows [Eq. (4)]:

$$-3.3\,eV \leq \mu_O - \mu_S \leq -2.1\,eV \tag{4}$$

We further considered the introduction of doped atoms. When a $La^{3+}$ ion (0.167, 0.833, 0.721) was replaced by an

alkali-metal ion ($Li^+$, $Na^+$ or $K^+$), a defect ($v_S^{\bullet\bullet}$ or $v_O^{\bullet\bullet}$) could be generated, as in a $2\times2\times1$ $La_2O_2S$ supercell. To neutralize the negative charge, an anion vacancy would arise. There are six different anion vacancies showed in Figure 3. For $La_2O_2S$, we selected two kinds of sulfur vacancies (A1, A2) and four different kinds of oxygen vacancies (B1, B2, C1, C2). Correspondingly, in the system with alkali-metal doping, the chemical-conversion relationship between M (Li, Na or K)-doped $La_2O_2S$ and $La_2O_3$ is shown below [Eq. (5)].

$$La_7O_7S_4M + 4O \rightarrow La_7O_{11}M + 4S \tag{5}$$

The phase boundary is still a straight line with a slope of 1 [Eq. (6)].

$$\mu_O = \mu_S + \frac{1}{4}[E_{tot}(La_7O_{11}M) - E_{tot}(La_7O_7S_4M)] \tag{6}$$

Herein, we focused on the moving of the upper boundary (i.e., $La_2O_3$/$La_2O_2S$) in the phase diagram. By means of DFT simulation, the total energies of alkali-metal-doped $La_2O_2S$ with different defects were calculated, and are given in Table 2.

**Table 2.** Total energy of alkali-metal-doped $La_2O_2S$ with defects.

| Anion vacancy site | Li-doped $La_2O_2S$ | | K-doped $La_2O_2S$ | |
| --- | --- | --- | --- | --- |
| | $E_{tot}$ [eV] | Type of vacancy | $E_{tot}$ [eV] | Type of vacancy |
| A1 | −145.5 | $v_S^{\bullet\bullet}$ | −144.5 | $v_S^{\bullet\bullet}$ |
| A2 | −144.7 | $v_S^{\bullet\bullet}$ | −143.8 | $v_S^{\bullet\bullet}$ |
| B1 | −143.5 | $v_O^{\bullet\bullet}$ | −142.4 | $v_O^{\bullet\bullet}$ |
| B2 | −142.5 | $v_O^{\bullet\bullet}$ | −141.7 | $v_O^{\bullet\bullet}$ |
| C1 | −143.1 | $v_O^{\bullet\bullet}$ | −142.0 | $v_O^{\bullet\bullet}$ |
| C2 | −142.9 | $v_O^{\bullet\bullet}$ | −142.0 | $v_O^{\bullet\bullet}$ |

By following a similar method, the total energies of doped $La_2O_3$ with oxygen vacancies were also acquired and are shown in Table 3.

Then the defect-formation energy of the most stable vacancy structure was chosen to calculate the phase boundary. The intercepts of the Li- and K-doped $La_2O_2S$/$La_2O_3$ interface were found to be −2.07 and −1.83 eV, respectively. These results were utilized to plot the phase diagrams of alkali-metal-doped systems in comparison with the undoped system (Figure 4).

From the phase diagram, the following conclusions can be drawn: 1) alkali-metal doping moves the phase boundary be-

**Table 3.** Total energy of alkali-metal-doped $La_2O_3$ with defects.

| Anion vacancy site | Li-doped $La_2O_2S$ | | K-doped $La_2O_2S$ | |
| --- | --- | --- | --- | --- |
| | $E_{tot}$ [eV] | Type of vacancy | $E_{tot}$ [eV] | Type of vacancy |
| A1 | −151.8 | $v_O^{\bullet\bullet}$ | −148.6 | $v_O^{\bullet\bullet}$ |
| A2 | −149.0 | $v_O^{\bullet\bullet}$ | −147.8 | $v_O^{\bullet\bullet}$ |
| B1 | −151.4 | $v_O^{\bullet\bullet}$ | −149.7 | $v_O^{\bullet\bullet}$ |
| B2 | −150.2 | $v_O^{\bullet\bullet}$ | −149.3 | $v_O^{\bullet\bullet}$ |
| C1 | −150.2 | $v_O^{\bullet\bullet}$ | −148.8 | $v_O^{\bullet\bullet}$ |
| C2 | −150.9 | $v_O^{\bullet\bullet}$ | −149.4 | $v_O^{\bullet\bullet}$ |
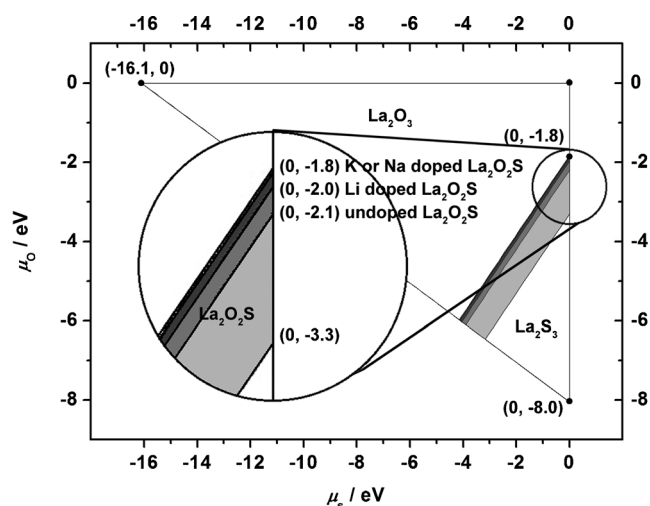


**Figure 4.** Phase diagram of $La_2O_3$, $La_2O_2S$, and $La_2S_3$. The phase boundary is a straight line with a slope equal to 1. The diagram in the circle shows a magnified distribution of doped and undoped $La_2O_2S$ NCs.

tween $La_2O_2S$ and $La_2O_3$ upwards. This indicates that doping could contribute to the stabilization of the $La_2O_2S$ phase; 2) the phase boundary shift for the Li-doped system is far less than that for the K-doped system. These calculation results are consistent with our experimental results, in which the Li doping was not as effective as K doping in facilitating the formation of $La_2O_2S$ NCs.

It is also noteworthy that since alkali-metal-doped $La_2O_2S$ has two kinds of defect vacancy, the relationship of the defect-formation energy between them determines the type of defect [Eq. (7)].

$$H_f(V_O^{\bullet\bullet}) - H_f(V_S^{\bullet\bullet}) = E_{La_2O_2S}(V_O^{\bullet\bullet}) - E_{La_2O_2S}(V_S^{\bullet\bullet}) + \mu_O - \mu_S \tag{7}$$

It has been mentioned that the stable conditions of $La_2O_2S$ NCs are described in Equation (4). The experimental results of Li and Na show that the defect-formation energy of the oxygen vacancy is always higher than that of the sulfur vacancy, which illustrates that the oxygen defect forms preferentially. However, the situation becomes different when K acts as the doping element. If $-3.3$ eV $\leq \mu_O - \mu_S \leq -2.2$ eV, the formation energy of the oxygen defect is higher than that of the sulfur defect. The conclusion remains unchanged. But in the case of a low chemical potential of sulfur ($-2.2$ eV $\leq \mu_O - \mu_S \leq -2.1$ eV), the calculation result demonstrates that the formation energy of sulfur may become higher instead and more sulfur vacancies would be generated.

If considering the above experimental and calculated results together (Tables 1 and 2), in comparison with the case of Na-doped $La_2O_2S$ NCs (La/Na 3.8:1 and La/S 2.6:1),[3h] the decreased contents of K and S atoms (La/K 16:1 and La/S 5.2:1) in K-doped $La_2O_2S$ NCs can be explained as follows: first, the reduction of the K content is possibly due to the influence of the radius of the doped cations. Since the radius of $K^+$ (1.38 Å, CN=6) is considerably larger than that of $La^{3+}$ (1.03 Å, CN=6) (which is relatively close to that of $Na^+$ (1.02 Å, CN=6)),[8] the

introduction of more $K^+$ ions to substitute $La^{3+}$ ions in $La_2O_2S$ NCs might increase the lattice distortion and thus limit the growth of the K-doped NCs. Under these conditions, a lower doping ratio of $K^+$ ions is beneficial to sustaining the hexagonal structure of the doped $La_2O_2S$ NCs. On the other hand, the inclusion of fewer S atoms in the K-doped $La_2O_2S$ NCs may be related to the Lewis acidity of the doping alkali-metal ions. The Lewis acidity of $K^+$ is somewhat stronger than that of $Na^+$, which causes an increased chemoaffinity between $K^+$ and $O^{2-}$. This leads to the production of a certain proportion of sulfur vacancies in K-doped $La_2O_2S$ NCs, as is disclosed by the above DFT calculation results. In this case, the presence of more sulfur vacancies in K-doped $La_2O_2S$ NCs will result in a decrease of the S content in the NCs.

Owing to its better capability in stabilizing hexagonal $La_2O_2S$ NCs compared with Li, K was chosen to explore its doping effect on the formation of the other rare-earth oxysulfide NCs (RE=Eu, Gd, Yb). The sizes, compositions, and shapes of the K-doped $RE_2O_2S$ NCs are also summarized Table 1. By comparing the TEM images (Figure 5) of different types of $RE_2O_2S$ NCs, it
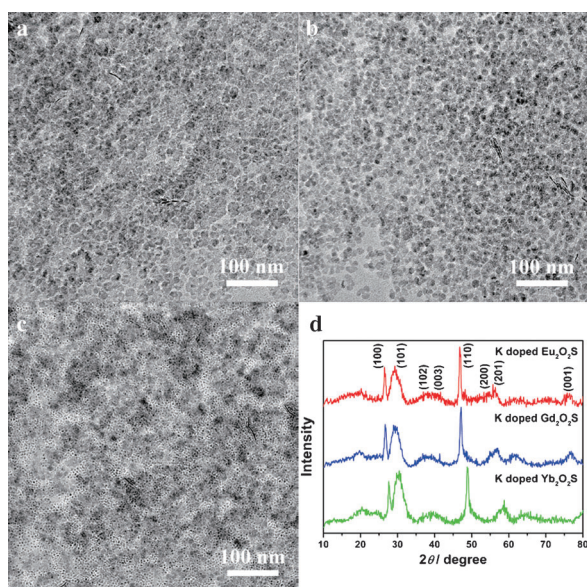
**Figure 5.** TEM images of a) K-$Eu_2O_2S$, b) K-$Gd_2O_2S$:Gd, and c) K-$Yb_2O_2S$ NCs. (d) XRD patterns of K-$RE_2O_2S$ (RE=Eu, Gd, Yb) NCs.

was discovered that as the radius of the rare-earth ion decreased, the size of the NCs became smaller (Table 1). For middle rare-earth elements (e.g., Eu and Gd), the morphology of $RE_2O_2S$ NCs transformed from hexagonal plates to irregular plates with a size of about 10 nm (Figure 5a,b). In addition, only small particles with a size of about 1 nm were formed for $Yb_2O_2S$ NCs under the same conditions (Figure 5c). For Lu, it was found that only $Lu_2O_3$ NCs could be formed (Figure S1 in the Supporting Information). The DFT calculations also agree with this result (Figure S2). In the phase diagrams of $RE_2O_3$, $RE_2O_2S$, and $RE_2S_3$, the phase-formation ability can be represented by the intercept between the phase interface and the $y$ axis. From La to Lu, the intercept is smaller and the formation of the $RE_2O_2S$ phase becomes more difficult at the same time.

The XRD patterns of different K-doped $RE_2O_2S$ NCs (Figure 5d) also demonstrate the tendency of the diffraction peaks to move to smaller angles from Eu to Gd and to Yb, which indicates the gradual lattice shrinkage of the NCs arising from the lanthanide contraction. The fitted unit-cell parameters are $a=$ 3.876 Å, $c/a=1.855$, $V=93.55$ Å$^3$ for $Eu_2O_2S$; $a=3.854$ Å, $c/a=$ 1.736, $V=86.06$ Å$^3$ for $Gd_2O_2S$; and $a=3.723$ Å, $c/a=1.782$, $V=$ 79.64 Å$^3$ for $Yb_2O_2S$. The EDS data of $RE_2O_2S$ NCs (Figure S3) show that the doping concentration of $K^+$ is always maintained at a relatively low level (RE/K lying between10:1 and 16:1) regardless of different rare-earth dopants, which is consistent with the previous discussion.

The stability of $RE_2O_2S$ NCs can be explained from the perspective of ionic radii. Firstly, the radius changes caused by $K^+$ doping increase from 25.4 to 56.8% along the lanthanide series, which leads to a larger degree of lattice distortion, which could hinder the formation of oxysulfide NCs for heavy rare-earth metals. Meanwhile the Lewis acidity might play an important role in that it becomes stronger as the ionic radius decreases from $La^{3+}$ to $Lu^{3+}$. This could lead to the fact that for heavy rare-earth ions, the affinity between rare-earth ions and $O^{2-}$ is much stronger than that between $RE^{3+}$ and $S^{2-}$. For example, for $Lu^{3+}$, only $Lu_2O_3$ NCs could be synthesized regardless of the introduction of the K dopant (Figure S1).

As is known, Eu- or Tb-doped $La_2O_2S$ are important phosphors of wide applications such as lighting and displays.[5] By following the synthetic method we developed, we also prepared monodispersed Eu/K- and Tb/K-codoped $La_2O_2S$ nanoplates in hexagonal structures (Figure 6 and Figure S4 and S5),
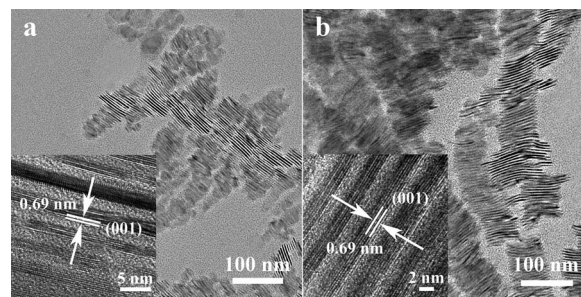
**Figure 6.** TEM and HRTEM (insets) images of a) K-$La_2O_2S$:4%Eu and b) K-$La_2O_2S$:1%Tb nanoplates.

and investigated their luminescent properties with commercial $La_2O_2S$:4%Eu and $La_2O_2S$:1%Tb bulk powders as references, respectively (Figure 7, and Figure S6–S8). As determined from the TEM images (Figure 5a,b), the sizes of the K-$La_2O_2S$:4%Eu and K-$La_2O_2S$:1%Tb nanoplates are ((59.2 ± 11.1) × (2.2 ± 0.1)) nm and ((43.3 ± 3.3) × (2.8 ± 0.2)) nm, respectively, which is significantly larger than those of the Na-doped ones.[3h] In addition, the nanoplates formed nanowire-like structures through the face-to-face self-assembly along the $c$ axis. The distance between two layers of nanoplates is about 3 nm, which is almost twice the length of an oleic acid molecule.[2d] By HRTEM observation, the as-obtained K-$La_2O_2S$:4%Eu and K-$La_2O_2S$:1%Tb nanoplates are only 6 layers of unit cells, so the nanoplates would have a certain flexibility, for which a bending
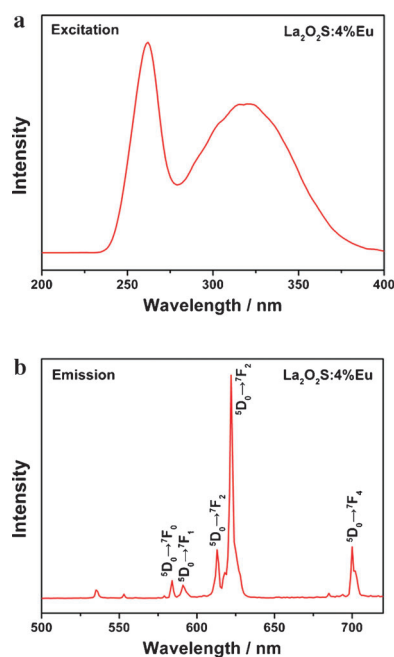
**Figure 7.** a) Fluorescence excitation spectrum and b) emission spectrum of K-La$_2$O$_2$S:4%Eu NCs dispersed in cyclohexane under 262 nm UV excitation.

phenomenon could be seen from the TEM images (Figure 6a,b).

Figure 7a shows the room-temperature excitation spectra of the K-La$_2$O$_2$S:4%Eu NCs with an emission of 622 nm of Eu$^{3+}$. The excitation band from 240 to 270 nm is ascribed to the charge transfer from O$^{2-}$ to Eu$^{3+}$, whereas the broad excitation band above 300 nm is assigned to the charge transfer from S$^{2-}$ to Eu$^{3+}$.[9a] We chose 262 nm UV light as the excitation wavelength and obtained the fluorescence emission spectrum of K-La$_2$O$_2$S:4%Eu NCs (Figure 7b). The spectrum is composed of a series of spectral lines at 500–750 nm, which were generated from the excited state $^5D_0$ to the $^7F_J$ ($J$=0, 1, 2, 4) level transition of Eu$^{3+}$. The strongest emission peak is situated at about 610–630 nm, which corresponds to the red light ($^5D_0 \rightarrow {}^7F_2$). The fluorescence colors of K-La$_2$O$_2$S:4%Eu NCs can be described on the *xy* chromaticity diagram as (0.64, 0.23), whereas the corresponding bulk material is (0.64, 0.35) and Eu/Na-codoped La$_2$O$_2$S is (0.58, 0.40). With excitation at 335 nm, the photoluminescence quantum yield (PLQY) of the K-La$_2$O$_2$S:4%Eu NCs was determined to be 12.4%, which is lower than that of bulk La$_2$O$_2$S:4%Eu (38.2%), but is much higher than that (4.3%) of the Eu/Na-codoped one.[3h] It is probably because K-La$_2$O$_2$S:4%Eu NCs have better crystallinity and larger crystalline size than the Eu/Na-codoped one. Under these conditions, the lattice relaxation caused by nonradiative transitions would be reduced and thus the PLQY was significantly enhanced for the K-La$_2$O$_2$S:4%Eu NCs. Na-doped La$_2$O$_2$S NCs, which had a small diameter and were thin, would lead to a faster energy transfer and dissipation through the nonradiative pathway.

The fluorescence emission spectrum of K-La$_2$O$_2$S:1%Tb NCs (Figure S8) was also obtained with UV excitation at 262 nm.

There are four peaks at 450–650 nm, which correspond to the transition from $^5D_4$ to $^7F_J$ ($J$=3, 4, 5, 6) of Tb$^{3+}$. The strongest peak is situated at about 530–560 nm, which corresponds to green light ($^5D_4 \rightarrow {}^7F_5$).[3f, 6]

The luminescence decay curves of Eu/K- and Tb/K-codoped La$_2$O$_2$S NCs can be fitted into a single-exponential function [Eq. (8)]:

$$I = I_0 e^{-t/\tau} \tag{8}$$

For Eu-doped La$_2$O$_2$S, $\tau$ is 623 µs for K-doped NCs (Figure S6), 640 µs for Na-doped NCs,[3h] and 340 µs for the bulk material; and for Tb-doped La$_2$O$_2$S, $\tau$ is 939 µs for K-doped NCs (Figure S7b), 1221 µs for Na-doped NCs,[3h] and 637 µs for the bulk material. It is probable that as a result of the decreasing radiative transition rates originating from the change in the effective refractive index on K- or Na-doped La$_2$O$_2$S, the luminescence lifetimes of both Eu/K- and Tb/K-codoped La$_2$O$_2$S NCs are longer than their bulk counterparts.[9]

## Conclusion

Hexagonal rare-earth oxysulfide nanocrystals doped with different alkali metals were synthesized by the thermolysis of metal acetyltacetonates in mixed organic solvents of OA, OM, and ODE in the presence of commercial sulfur powders. Through a combination of controlled experiments and first-principles calculations, the influences of alkali-metal dopants (Li, Na, K) on the controlled synthesis process of the rare-earth oxysulfide NCs were revealed as 1) the doping of alkali metals to substitute rare-earth cations can affect the size, shape, crystallinity, composition, and phase stability of the RE$_2$O$_2$S NCs; 2) similar to Na, but much better than Li, K could effectively stabilize the hexagonal structure of the RE$_2$O$_2$S NCs. DFT calculations further indicated that different alkali-metal dopants can change the stabilities of O and S vacancies in the hexagonal lattice of RE$_2$O$_2$S, which resulted in the ratio changes of cations to S$^{2-}$ anions, consistent with experimental results. By the same approach, Eu/K- and Tb/K-codoped La$_2$O$_2$S NCs were also synthesized, which showed strong red and green emissions under UV excitation. This research combining experimental control and theoretical calculations has shed new light on the fundamental exploration of controlled synthesis and the related mechanism of rare-earth compound nanocrystals, and has demonstrated further a powerful and practical strategy for tuning the phase stability, nanostructure features, and material properties of various inorganic nanocrystals of important applications.

## Experimental Section

### Synthesis of alkali-metal-doped RE$_2$O$_2$S nanocrystals (NCs)

In a typical synthesis, [RE(acac)$_3$] (0.5 mmol), [M(acac)] (M=Li, K) (0.5 mmol), S (1.0 mmol), OA (2.5 mmol), OM (17 mmol), and ODE (20 mmol) were loaded in a three-necked flask (100 mL) at RT. The mixture was heated to 120 °C under vacuum for 30 min to remove water and other impurities with low boiling points. The solution was then heated to 310 °C at a heating rate of 20 °C min$^{-1}$ under

a high-purified $N_2$ atmosphere. The solution generally turned from turbid to transparent at about 240 °C during the heat-up process. After 30 min of reaction, the solution was air-cooled to RT and NCs were precipitated from the crude solution by ethanol, followed by centrifugation and dispersion in cyclohexane. Finely adjusting the amount of [M(acac)] led to different thicknesses and sizes of the nanoplates. Furthermore, when the amount of OA was increased from 2.5 to 5 mmol while maintaining the amount of all the other components, the solution turned milky when kept at 310 °C for 10 min. The as-synthesized NCs self-assemble in solution to form nanowires of several hundred nanometers.

### X-ray diffraction

The powder XRD patterns were characterized on a Rigaku D/MAX-2000 diffractometer (Japan) with a slit of 1/2° at a $2\theta$ scanning speed of 8° min$^{-1}$ under Cu$_{K\alpha}$ radiation ($\lambda = 1.5406$ Å).

### Transmission electron microscopy

Samples for TEM analysis were prepared by drying a drop of diluted colloid solution of doped $RE_2O_2S$ nanocrystals in cyclohexane on copper grids coated with amorphous carbon. HRTEM, EDS, and SAED analyses were performed on a FEG-TEM instrument (JEM-2100F, JEOL, Japan) operated at 200 kV.

### Photoluminescence

The UV-simulated photoluminescence (PL) properties of Eu/K- and Tb/K- codoped $La_2O_2S$ nanocrystals were measured at RT on a Hitachi F-4500 fluorescence spectrophotometer (Japan) with a xenon lamp as a stimulation source. The scanning speed was fixed at 60 nm min$^{-1}$ with both the excitation and emission splits fixed at 2.5 nm. The lifetime measurements of the nanoplates were obtained on an Edinburgh Instruments FLS920 transient/steady-state fluorescence spectrometer at RT. The PL quantum yields of the nanocrystals were measured by the absolute method using the integrating sphere of the Horiba Jobin Yvon Nanolog system. The co-ordinates in the $xy$ chromaticity diagram are directly calculated from the fluorescence spectra (CIE 1931).

## Acknowledgements

[1] a) J.-C. G. Bünzli, *Chem. Rev.* **2010**, *110*, 2729; b) S. V. Eliseeva, J.-C. G. Bünzli, *Chem. Soc. Rev.* **2010**, *39*, 189; c) F. Wang, X. Liu, *Chem. Soc. Rev.* **2009**, *38*, 976; d) G. Wang, Q. Peng, Y. Li, *Acc. Chem. Res.* **2011**, *44*, 322.

[2] a) C. Y. Cao, *J. Am. Chem. Soc.* **2004**, *126*, 7456; b) R. Si, Y. W. Zhang, L. P. You, C. H. Yan, *Angew. Chem.* **2005**, *117*, 3320; *Angew. Chem. Int. Ed.* **2005**, *44*, 3256; c) R. Si, Y.-W. Zhang, H.-P. Zhou, L.-D. Sun, C.-H. Yan, *Chem. Mater.* **2007**, *19*, 18–27; d) Y. W. Zhang, X. Sun, R. Si, L. P. You, C. H. Yan, *J. Am. Chem. Soc.* **2005**, *127*, 3260; e) X. Sun, Y. W. Zhang, Y. P. Du, Z. G. Yan, R. Si, L. P. You, C. H. Yan, *Chem. Eur. J.* **2007**, *13*, 2320; f) Y. P. Du, Y. W. Zhang, L. D. Sun, C. H. Yan, *J. Phys. Chem. C* **2008**, *112*, 405; g) Y. P. Du, Y. W. Zhang, Z. G. Yan, L. D. Sun, C. H. Yan, *J. Am. Chem. Soc.* **2009**, *131*, 16364; h) Y. P. Du, Y. W. Zhang, L. D. Sun, C. H. Yan, *J. Am. Chem. Soc.* **2009**, *131*, 3162.

[3] a) J. C. Boyer, F. Vetrone, L. A. Cuccia, J. A. Capobianco, *J. Am. Chem. Soc.* **2006**, *128*, 7444; b) H. X. Mai, Y. W. Zhang, R. Si, Z. G. Yan, L. D. Sun, L. P. You, C. H. Yan, *J. Am. Chem. Soc.* **2006**, *128*, 6426; c) G. S. Yi, W. B. Lee, G. M. Chow, *J. Nanosci. Nanotechnol.* **2007**, *7*, 2790; d) T. Mirkovic, M. A. Hines, P. S. Nair, G. D. Scholes, *Chem. Mater.* **2005**, *17*, 3451; e) R. S. Selinsky, J. H. Han, E. A. M. Perez, I. A. Guzei, S. Jin, *J. Am. Chem. Soc.* **2010**, *132*, 15997; f) F. Zhao, M. Yuan, W. Zhang, S. Gao, *J. Am. Chem. Soc.* **2006**, *128*, 11758; g) F. Zhao, S. Gao, *J. Mater. Chem.* **2008**, *18*, 949; h) Y. Ding, J. Gu, J. Ke, Y. W. Zhang, C. H. Yan, *Angew. Chem.* **2011**, *123*, 12538; *Angew. Chem. Int. Ed.* **2011**, *50*, 12330; i) Y. Ding, J. Gu, T. Zhang, A. X. Yin, L. Yang, Y. W. Zhang, C. H. Yan, *J. Am. Chem. Soc.* **2012**, *134*, 3255; j) J. Gu, Y. Ding, J. Ke, Y. W. Zhang, C. H. Yan, *Acta Chim. Sin.* **2013**, *71*, 360.

[4] R. G. Pearson, *J. Am. Chem. Soc.* **1963**, *85*, 3533; R. G. Pearson, *Science* **1966**, *151*, 172.

[5] R. Vali, *Comput. Mater. Sci.* **2006**, *37*, 300.

[6] a) J. Dhanaraj, M. Geethalakshmi, R. Jahannathan, T. R. N. Kutty, *Chem. Phys. Lett.* **2004**, *387*, 23; b) H. S. Peng, S. H. Huang, F. T. You, J. J. Chang, S. Z. Lu, L. Cao, *J. Phys. Chem. B* **2005**, *109*, 5774; Z. Liu, X. Sun, J. Lian, X. Li, Z. Xiu, Q. Li, D. Huo, J. G. Li, *J. Phys. Chem. C* **2008**, *112*, 2353.

[7] a) S. B. Zhang, J. E. Northrup, *Phys. Rev. Lett.* **1991**, *67*, 2339; b) S. H. Wei, S. B. Zhang, A. Zunger, *J. Appl. Phys.* **1999**, *85*, 7214.

[8] R. D. Shannon, *Acta Crystallogr., Sect. A* **1976**, *32*, 751.

[9] a) Q. L. Dai, H. W. Song, M. Y. Wang, X. Bai, B. Dong, R. F. Qin, X. S. Qu, H. Zhang, *J. Phys. Chem. C* **2008**, *112*, 19399; b) B. Henderson, G. Imbusch, *Optical Spectroscopy of Inorganic Solids*, Clarendon Press, Oxford, **1989**, p. 173.